

NUMERICAL INVESTIGATION OF A BLUFF BODY STABILIZED TURBULENT PREMIXED FLAME WITH LARGE EDDY SIMULATION

Yagiz Yalcinkaya*, Ogeday E. Bozkurt† and Ayse G. Gungor‡
Istanbul Technical University
Istanbul, Turkey

ABSTRACT

In this study, reacting and non-reacting turbulent flows around a bluff body that experimental researches executed by the Air Force research laboratory are simulated with large eddy simulation approach using an open source flow solver, OpenFOAM. Premixed combustion of propane-air mixture is performed with Partially Stirred Reactor combustion model by using two different global reaction mechanisms. Both non-reacting and reacting flow results agree well with the experimental and numerical data. It is observed that the reaction suppresses the Kelvin-Helmholtz instability, wall-vortex interaction, and extends the re-circulation zone. According to mean and rms axial velocity and temperature distributions, results show that there are no crucial changes between different grids and reaction mechanisms.

INTRODUCTION

Efficiencies of engines are directly related with combustion mechanisms. The efficiency of combustion mechanisms varies depending on the airflow, evaporation, reaction or mixing rate values [Lefebvre et.al., 2010]. Flame stabilization is one of the common methods that are used for achieving an efficient combustion mechanism with increasing mixing rate. Main goal of stabilizing the flame is not only decreasing the flow speed to flame speed but also increasing the flame speed to flow speed at the same time to facilitate ignition [Lefebvre et.al., 2010]. Many techniques are used for stabilizing the flame, such as backward facing step, swirl and triangular bluff body [Manickam et.al., 2012]. Bluff bodies are structures that form periodic vortexes in order to stabilize the flame. There are many researches about behavior of these vortexes formed behind flame holder, not only experimentally but also numerically.

Experimental studies on flow over bluff body structure are conducted for long years, but numerical methods become more widespread with improved high performance computers. Mainly these studies aim to observe the wake region and vortexes, which are difficult to solve numerically. That's why, many researches that examine the flow behind bluff body structures, encounter some inconsistencies that are primarily caused by the turbulence method [Manickam et.al., 2012],[Bai et.al., 1994]. Large eddy simulation (LES), which is successful in resolving these critical regions of flow is used for the

*BS Student, in Department of Aeronautical Engineering, Email: yalcinkayay16@itu.edu.tr

†BS Student, in Department of Aeronautical Engineering, Email: bozkurto16@itu.edu.tr

‡Assoc. Prof, in Department of Astronautical Engineering, Email: ayse.gungor@itu.edu.tr

simulations presented in this study. LES is a method based on resolving the geometrically dependent large scales of the flows and modeling the smaller scales. LES provides both efficient solution in terms of time than direct numerical simulation (DNS) and smaller modeling error than Reynolds-averaged Navier-Stokes. In this study, Partially Stirred Reactor (PaSR) combustion model, which is derived from behavior of turbulent mixing and combustion provided by experimental and DNS data is utilized [Sabelnikov et.al., 2013].

This study is carried out to examine the wake zone, vortex structures formed behind the flame holder, and effect of the reaction on these structures by performing reacting and non-reacting analysis of a flow around a triangular bluff body. LES methodology with Smagorinsky sub-grid model and PaSR combustion model is used for the analysis conducted in an open source flow solver OpenFOAM. Both non-reacting and reacting flows analyses are presented in this paper. Effects of the bluff body on the spatial development of the flow, the reaction mechanisms and grid are investigated and compared with experimental and numerical results.

NUMERICAL METHODS

Mathematical Approach

The LES turbulence approach applied here is based on implicitly low-pass filtered equations of mass, momentum, and energy. The low-pass filtering extracts the resolved scale components from the subgrid scale components, which is smaller than the filter width (Δ) and small scales are modelled by SGS model. For mass, momentum, total energy and species transport, LES equations are given as:

$$\frac{\partial \bar{\rho}}{\partial t} + \frac{\partial}{\partial x_i}(\bar{\rho} \tilde{u}_i) = 0 \quad (1)$$

$$\frac{\partial \bar{\rho} \tilde{u}_i}{\partial t} + \frac{\partial}{\partial x_j}(\bar{\rho} \tilde{u}_i \tilde{u}_j) = -\frac{\partial \bar{p}}{\partial x_i} + \frac{\partial}{\partial x_j}(\bar{\tau}_{ij} - \bar{\rho}(\tilde{u}_i \tilde{u}_j - \tilde{u}_i \tilde{u}_j)) \quad (2)$$

$$\frac{\partial \bar{\rho} \tilde{h}}{\partial t} + \frac{\partial}{\partial x_i}(\bar{\rho} \tilde{u}_i \tilde{h}) = \frac{D\bar{p}}{Dt} + \frac{\partial}{\partial x_i}(\lambda \frac{\partial \tilde{h}}{\partial x_i} - \bar{\rho}(\tilde{u}_j \tilde{h} - \tilde{u}_j \tilde{h})) + \dot{w}_T \quad (3)$$

$$\frac{\partial \bar{\rho} \tilde{Y}_k}{\partial t} + \frac{\partial}{\partial x_i}(\bar{\rho} \tilde{u}_i \tilde{Y}_k) = \frac{\partial}{\partial x_i}(\bar{\rho} \tilde{D}_k \frac{\partial \tilde{Y}_k}{\partial x_i} - \bar{\rho}(\tilde{u}_j \tilde{Y}_k - \tilde{u}_j \tilde{Y}_k)) + \tilde{w}_k \quad (4)$$

In these equations, tilde denotes Favre-filtering while overbar denotes spatial filtering. Here, $\bar{\rho}$, \tilde{u}_i , \tilde{h} , \tilde{Y}_k , $\bar{\tau}_{i,j}$, are the filtered density, i -th velocity component, enthalpy, species mass fractions of k^{th} species and stress tensor respectively. D_k is the dissipation parameter of k^{th} species, \dot{w}_T is the heat release in reaction, \tilde{w}_k is filtered reaction rate, and λ is thermal conductivity. In the filtered equations, unclosed terms appear as unresolved Reynolds stress $\tau_{ij}^{sgs} = \bar{\rho}(\tilde{u}_i \tilde{u}_j - \tilde{u}_i \tilde{u}_j)$, enthalpy flux $\bar{\rho}(\tilde{u}_j \tilde{h} - \tilde{u}_j \tilde{h})$, species flux $\bar{\rho}(\tilde{u}_j \tilde{Y}_k - \tilde{u}_j \tilde{Y}_k)$ and these terms require subgrid modeling.

Unresolved Reynolds stress is written as $\tau_{ij}^{sgs} = -2\nu_\tau \tilde{S}_{ij} + \tau_{kk} \frac{1}{3} \delta_{ij}$ by correlating turbulent eddy viscosity with Boussinesq assumption. In which, ν_τ is turbulent eddy viscosity associated with the product of the velocity scale and a length scale, δ_{ij} is Kronecker delta and τ_{kk} is isotropic contribution. Smagorinsky sgs model is used to calculate turbulent eddy viscosity, which is expressed as:

$$\nu_\tau(x, t) = (C_s \bar{\Delta})^2 \tilde{S}_{ij} \quad (5)$$

Here, C_s is Smagorinsky coefficient with value equal to 0.158, $\bar{\Delta}$ is the filter width corresponding to the length scale size and \tilde{S}_{ij} is the filtered strain rate tensor, $\tilde{S}_{ij} = \frac{1}{2}(\frac{\partial \tilde{u}_i}{\partial x_j} + \frac{\partial \tilde{u}_j}{\partial x_i})$. To solve the remaining unclosed filtering equations, turbulent viscosity is also used. The unresolved enthalpy and species flux terms are modeled using the turbulent viscosity approach, as, respectively:

$$\bar{\rho}(\widetilde{u_j h} - \tilde{u}_j \tilde{h}) = -\frac{\nu_\tau}{Pr_t} \frac{\partial \bar{h}}{\partial x_i}, \quad (6)$$

$$\bar{\rho}(\widetilde{u_j Y_k} - \tilde{u}_j \tilde{Y}_k) = -\frac{\nu_\tau}{Sc_t} \frac{\partial \tilde{Y}_k}{\partial x_i}. \quad (7)$$

Here, Sc_t is the turbulent Schmidt number and Pr_t is the turbulent Prandtl number.

The filtered reaction rates are modeled using the Partially Stirred Reactor LES model in this study (LES-PaSR). This method works with the analogy of splitting the computational cell into two parts that characterize reacting and non-reacting parts [Sabelnikov et.al., 2013]. The reaction zone serves as a stirred reactor in which all species are properly stirred and reacted with each other. Because of turbulent effects caused by mixing time (τ_{mix}), new species calculated in the reaction part mixes the whole domain [Ferrarotti et.al., 2018]. In the PaSR combustion model, the mass fraction of reaction zone is expressed as:

$$\kappa = \frac{\tau_c}{\tau_c + \tau_{mix}}. \quad (8)$$

Here, the chemical time-scale, τ_c , is defined as $\tau_c \approx \delta_u/s_u$, where δ_u and s_u are the laminar flame thickness and flame speed, respectively. Also, τ_{mix} represents characteristic mixing time. Then, the cell's filtered reaction rate is defined as:

$$\bar{w}_k = \kappa \frac{\bar{\rho}(Y_i^* - Y_i^0)}{\tau^*}, \quad (9)$$

where τ^* is the residence time that needs to be modeled to achieve a closed set of equations [Zettervall et.al., 2017]. The modeling of τ^* is based on the assumption that the dissipative length scale (ℓ_D) gives the fine structure area-to-volume ratio [Sabelnikov et.al., 2013]. The dissipative length scale, $\ell_D = (\nu\Delta/v')^{1/2}$ defined by viscosity (ν) and the subgrid velocity stretch (v'/Δ) where v' is the subgrid velocity fluctuations, and that the velocity interfering with these structures is Kolmogorov velocity, $v_k = (\nu\epsilon)^{1/4}$, so that $\tau^* = \ell_D/v_k$ [Zettervall et.al., 2017]. The mass fraction of species in the reaction zone is represented by Y_i^* , whereas the mass fraction of species in the non-reacting zone is represented by Y_i^0 [Iavarone et.al., 2020].

As mentioned in several numerical studies, e.g. [Bulat et.al., 2015] [Pope et.al., 2014], the reaction mechanism is key to the success of an LES computation. Detailed and skeletal reaction mechanisms can accurately predict combustion properties such as flame speed, ignition delay time, flame temperature and extinction strain-rate, since they include many intermediate steps [Zettervall et.al., 2017]. Despite the advantages of these reaction mechanisms, they result in huge computational cost in numerical studies. Therefore, one-step and two-step global reaction mechanisms that can simulate reacting flow without high computational cost are used for modelling propane reaction in the study [Westbrook and Dryer, 1981]. The details of the one step and two step reaction mechanisms for C₃H₈ combustion, named as WD-1 and WD-2, respectively are given in Table 1 [Westbrook and Dryer, 1981]. Reaction rate is calculated using the Arrhenius law, which is stated as:

$$k = AT^\beta \exp\left(\frac{E_a}{RT}\right) [C_3H_8]^a [O_2]^b. \quad (10)$$

Here, A is the exponential factor, β is the temperature exponent, R is the universal gas constant, a and b are the concentration exponents, and E_a is the activation energy which expresses the minimum energy required for the combustion to start.

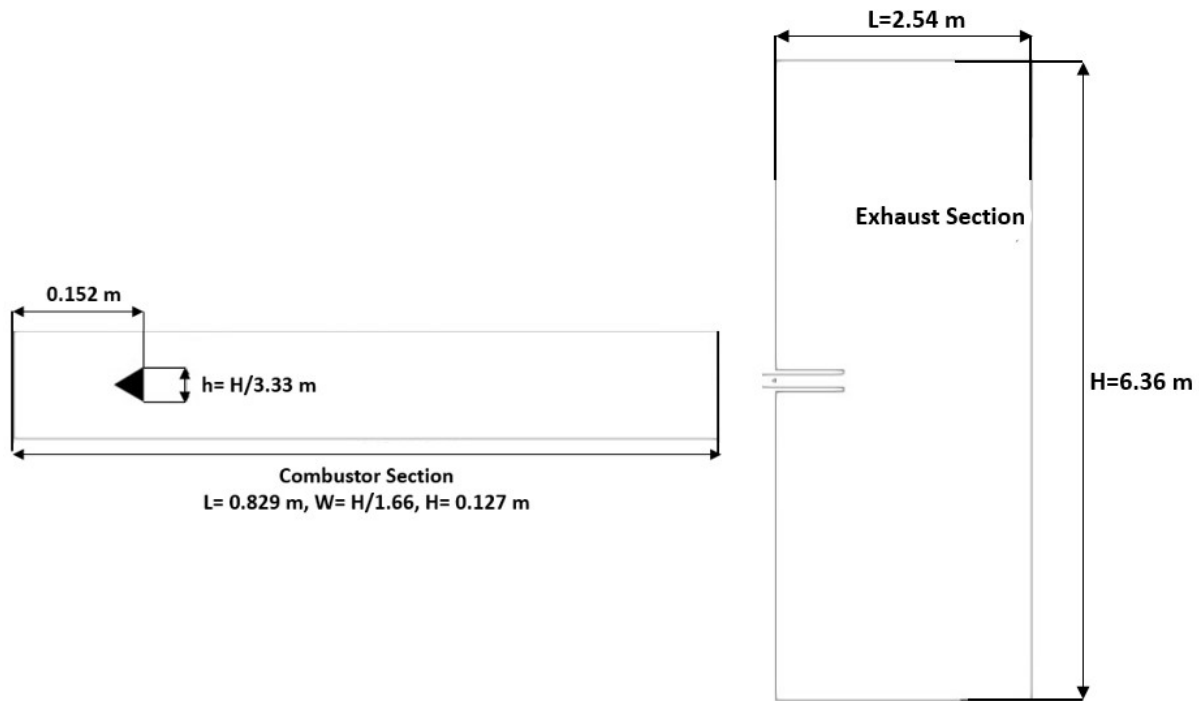
Table 1: WD-1 and WD-2 global reaction mechanisms used for C₃H₈ combustion under air-fuel conditions (Units are in m-sec-kmol-J-K).

Reaction No	Reaction	A	E_a	β	Reaction Orders
WD-1	$C_3H_8 + 5O_2 + 18.8N_2 \rightarrow 3CO_2 + 4H_2O + 18.8N_2$	4.836×10^9	2×10^8	0	$[C_3H_8]^{0.1}[O_2]^{1.65}$
WD-2-1	$C_3H_8 + 3.5O_2 + 18.8N_2 \rightarrow 3CO + 4H_2O + 18.8N_2$	5.62×10^9	1.25×10^8	0	$[C_3H_8]^{0.1}[O_2]^{1.65}$
WD-2-2f	$CO + 0.5O_2 \rightarrow CO_2$	2.24×10^{12}	1.67×10^8	0	$[CO]^1[O_2]^{0.25}[H_2O]^{0.5}$
WD-2-2r	$CO_2 \rightarrow CO + 0.5O_2$	5×10^8	1.67×10^8	0	$[CO_2]^1$

Geometry

This study is conducted with two geometries. For the non-reacting flow analysis the AFRL geometry, which includes combustor and exhaust is used [AIAA SciTech, 2020]. On the other hand, reacting flow analysis are focused on only combustor section of the AFRL geometry.

The combustor consists of a rectangular tunnel and an equilateral triangular bluff body. Dimensions of the combustor are $21.75h$ in channel length, $3.33h$ in height, and $2h$ in width, where $h = 0.0381m$ is the length of the bluff body edge. The vertical length of the exhaust section is $6.36m$ and the horizontal length from the back of the flame holder to the exit domain is $2.54m$. The combustor part of the geometry and exhaust are shown in Figure 1.

**Figure 1:** Schematic view of geometry. Left: Combustor section, right: Exhaust section

Mesh Details

For the non-reacting flow case, three types of meshes are generated. While creating the mesh, it is aimed to capture the behavior of the flow by condensing the mesh in the wake region formed behind the flame holder as well as the region where flow travels along with the exhaust domain. Fine mesh is densified in all directions, but medium-mesh has a lower resolution in wall-normal direction and coarse mesh consists of lower mesh resolution in both axial and wall-normal directions as compared with the fine mesh. The details and quality of the mesh for the non-reacting flow analysis are presented in Table 2.

Table 3 presents the mesh details for the combustor only set-up which is used for the reacting flow analysis. Both meshes contain the same density in the wall-normal and transverse direction but the “fine only-combustor” has more resolution than the medium mesh, in the axial direction.

Table 2: Grid quality of combustor and exhaust set-up for the non-reacting flow analysis.

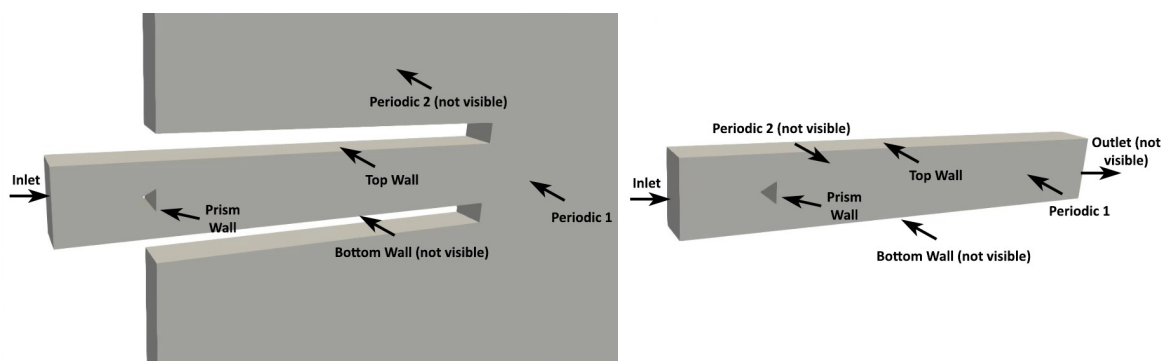
	Coarse Mesh	Medium Mesh	Fine Mesh
Max. Aspect Ratio	46.0268	43.2287	27.7151
Max. Non-orthogonality	29.8338 (avg.:3.1041)	27.8338 (avg. :3.2409)	29.8338 (avg. :2.41647)
Max. Skewness	0.54241	0.73812	0.72434
Number of Cells	2 million	4.6 million	8.6 million

Table 3: Grid quality of combustor only set-up for the reacting flow analysis.

	Medium Only-Combustor Mesh	Fine Only-Combustor Mesh
Max. Aspect Ratio	14.4209	21.0654
Max. Non-orthogonality	29.8338 (avg.:4.83917)	29.8338 (avg.:4.83917)
Max. Skewness	0.724344	1.44281
Number of Cells	2.2 million	4.3 million

Boundary Conditions and Numerical Setup

As already mentioned, two different types of simulations are conducted with two different geometry. Boundary conditions for these two different set-ups, are shown in Figure 2, and given in Table 4. As seen from Table 4, although non-reacting and reacting flow have differences, they both have common conditions. In addition to the 16.6 m/s velocity inlet condition for both flows, the periodic boundary condition is used for the back and front walls. Besides these boundary conditions, no-slip condition is used on the bluff body and upper and lower walls for non-reacting and reacting flows. As the boundary conditions for non-reacting flow, inflow-outflow boundary condition is utilized for velocity and 100 kPa is used for pressure in the exit domain. With the addition of combustion physics, boundary conditions are changed for reacting flow. At the outlet boundary, a pressure wave transmissive boundary condition is used for pressure and the outlet temperature is set to 300 K. Unlike the non-reacting flow case, propane/air is included with an equivalence ratio of 0.65 as the inlet condition and the inlet temperature is set to 310 K. In addition, a film effect is generated by applying a temperature of 300 K to the upper and lower walls in order to prevent flame accumulation in the combustor.

**Figure 2:** Boundary conditions. Left: Non-reacting flow, right: Reacting flow.

For reacting flows, ignition process is important to obtain a proper performance and prevent flame blow off [Salvador et.al., 2013]. Two different ignition methods named injection and hot-spot, are studied for ignition process. In the hot spot ignition method, flame stability is ensured by a hot spot generated at 0.16m away from the inlet. The hot spot is a sphere that has 1600K temperature

Table 4: Boundary conditions for non-reacting and reacting cases.

Boundary Conditions		
BCs	Non-Reacting Flow	Reacting Flow
Inlet Premixed Fuel/ Oxidizer	-	Premixed Propane/Air
Inlet Equivalence Ratio	0	0.65
Inlet Mass Flow Rate	0.1819 kg/s	0.1819 kg/s
Inlet Stagnation Temperature	-	310 K
Inlet Velocity Profile	Uniform Steady Flow	Uniform Steady Flow
Inlet Turbulence Intensity	0	0
Bluff Body Surface Temperature	-	Adiabatic
Bluff Body Surface Velocity	No-Slip	No-Slip
Top &Bottom Combustor Wall Temperature	-	300 K
Top &Bottom Combustor Wall Velocity	No-Slip	No-Slip
Front and Back Patches	Periodic	Periodic
Exit Domain	Inflow/Outflow, 100 kPa	-
Exit of Combustor	-	Inflow/Outflow ,zeroGradient (T), waveTransmissive (p)

and 0.035m radius. After providing flame stability with the hot-spot method, the injection method is also studied. In this method, ignition is provided by injecting enthalpy from a determined point between a certain time. Although the injection ignition method is more complex than the hot spot method, it provides an advantage for flame stabilization, because the ignite time is determined. With a few trials, flame stability is also achieved with the injection method. Details of the ignition methods that provide flame stability are shown in Table 5.

Table 5: Details of Ignition methods.

Ignition Method			
Hot-spot		Injection	
Ignition location (center)	(0.16 0.06 0.015)	Ignition Location (center)	(0.16 0.06 0.015)
Ignition region (radius)	0.035 m	Ignition region (radius)	0.035 m
Field temperature value	1600 K	Enthalpy value	2E+08 J/kg
-	-	Start time	4 ms
-	-	Finish time	8 ms

Reacting and non-reacting analyzes are solved with the help of OpenFOAM which is an open source solver. As the pressure-velocity coupling algorithm, PISO and PIMPLE algorithms are used for non-reacting and reacting flow, respectively. While time step is applied for non-reacting as 5e-6 sec, the time step was reduced to 3e-6 sec for reacting flow in order to provide numerical stability by reducing CFL number. Reaction effect on the flow is examined with different reaction mechanisms. Also, effect of grid and reaction mechanism over the flow is investigated. All results are compared with experimental [AIAA SciTech, 2018] and numerical data [Fureby, 2019]. Simulations are performed with 56 cores at the National Center for High Performance Computing (UHeM) of Turkey. 80000 CPU-time were spent for reacting flow and 20000 CPU-time for non-reacting flow.

RESULTS

Results of the analysis are examined both statistically and physically for the purpose of verification and observing the behavior of both non-reacting and reacting flows. Results are both verified with experimental and numerical data. Besides verification of the results, the effect of reaction on the flow is examined for different meshes and reaction mechanisms.

In order to check the accuracy of the simulation, the probe data that is located at the shear layer is stored and analyzed. The energy density spectrum of the axial velocity as a function of frequency is shown in Figure 3 for both non-reacting and reacting flow cases. These two figures show that LES energy spectrum agrees well with Kolmogorov's power law, which indicates $-5/3$ decay in the inertial sub-range. The vortex shedding frequency and corresponding Strouhal number are compared with literature and shown in Table 6. Results show strong compatibility for both vortex shedding frequency and Strouhal number.

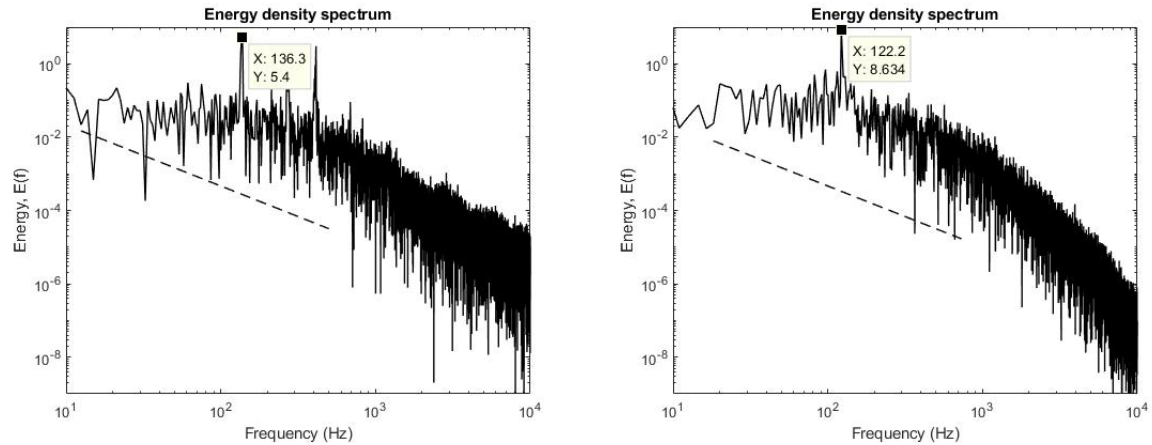


Figure 3: Energy density spectrum of axial velocity. Left one: Reacting flow, right one: Non-reacting flow.

Table 6: Comparison of Vortex shedding frequencies and Strouhal numbers with experimental and numerical studies [Sjunnesson et.al., 1992], [Giacomazzi et.al., 2004], [Porumbel et.al., 2006].

	<i>Vortex Shedding Frequency</i>		<i>Strouhal number</i>	
	<i>Non-reacting</i>	<i>Reacting</i>	<i>Non-reacting</i>	<i>Reacting</i>
<i>Simulation</i>	122.2	136.3	0.28	0.313
<i>Literature</i>	105	138.57-140	0.25	0.319-0.323

Correct prediction of the vortical structures formed behind the bluff body are extremely important due to their importance for flame stabilization, which is indeed the purpose of this geometry. In order to identify the vortical structures, Q-criterion technique is used. Figure 4 shows the coherent structures behind the bluff body by taking Q criterion as 150000 s^{-1} for both reacting and non-reacting flows. These vortical structures are colored with instantaneous axial velocity. In non-reacting flow, the shear layer instability leads to Kelvin-Helmholtz vortices. These vortices interact with the vortices generated at the walls of the combustor. However in reacting flow due to the acceleration of the flow and generation of the baroclinic torque, Kelvin-Helmholtz instabilities and wall-vortex interactions are suspended [Porumbel et.al., 2006]. Finally, reacting flow accelerates at the exhaust of the channel owing to temperature effect and expansion of the flow.

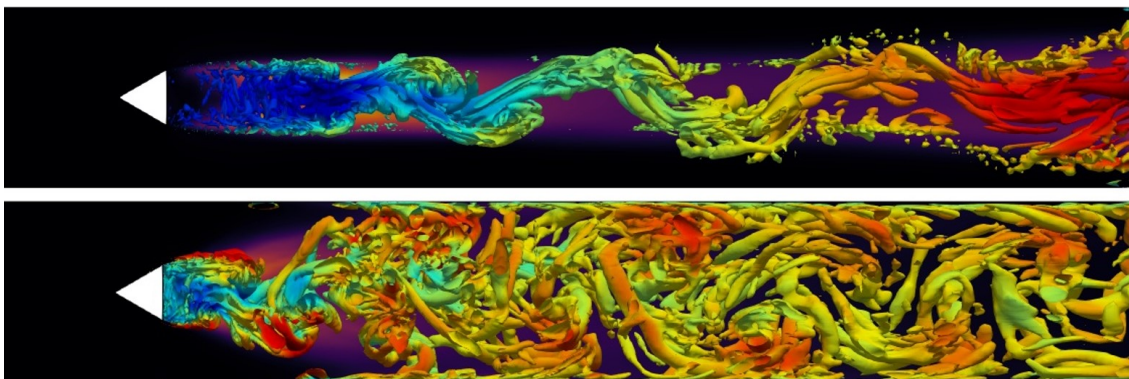


Figure 4: Iso-surface of coherent structures colored by the instantaneous axial velocity. Top: Reacting flow, bottom: Non-reacting flow.

Another crucial examination is the comparison of the turbulence statistics with experimental [AIAA SciTech, 2018] and numerical data [Fureby, 2019]. Statistics are collected for eight flow-through-time (FTT) after an initial transient of four FTT. The collected data are normalized with U_{bulk} , which is $16.6m/s$ and characteristic length of the flame holder ($D = 38.1mm$). Figure 5 presents the mean axial velocity and anisotropy along the centerline of the combustor for both reacting and non-reacting flows. According to Figure 5, the length of the re-circulation zone for non-reacting flow case is captured successfully. For reacting flow, as we can observed from the figure the re-circulation extends through to $x/D = 3.75$. Extension of the re-circulation zone is captured successfully but, there is an inconsistency on the strength of the reverse flow. This inconsistency might be due to low mesh resolution or global reaction mechanisms do not adequately reflect the physics of combustion. Same results are valid for anisotropy, which has a peak at the end of the re-circulation zone and is suppressed suddenly after that point because of the decreased wall-normal fluctuations. Although there are some inconsistencies with experimental data, all LES results obtained with different meshes and reaction mechanism agree well with experimental results.

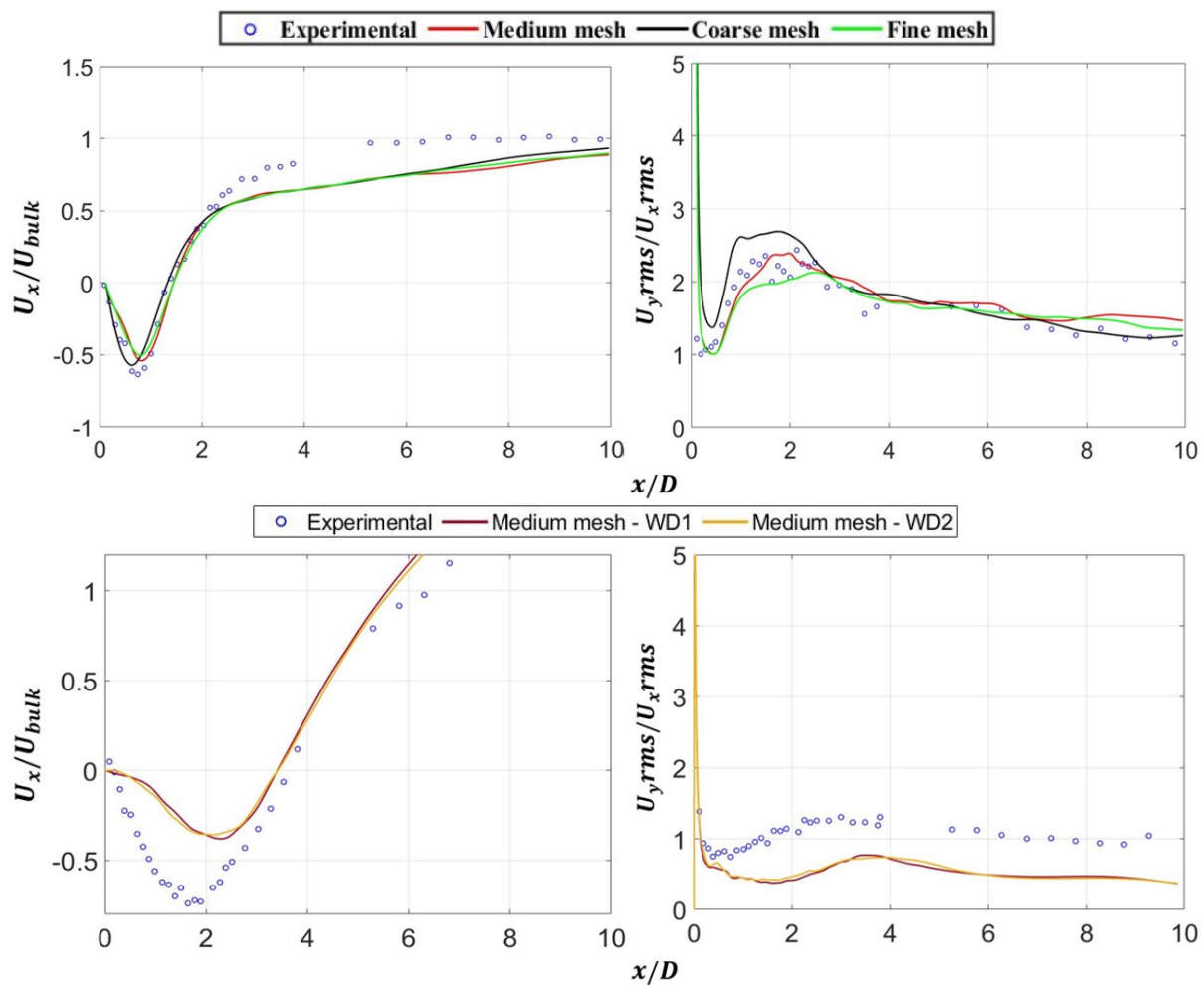


Figure 5: Normalized mean axial velocity (left) and anisotropy (right) distributions on the centerline along the flow path. Top: Non-reacting flow, bottom: Reacting flow.

In order to verify the general characteristics of reacting flow and observe effects of the grid and reaction mechanisms, temperature distributions are examined and compared with experimental and numerical data in Figure 6. The temperature values are normalized with adiabatic temperatures T_{ad} , which is equal to $1800K$ [Fureby, 2019] [Salvador et.al., 2013]. The mean temperature distribution shows that general behavior of the temperature captured well, but it does not increase smoothly as in experimental and numerical data. This might be due to mesh quality and reaction. The same situation is valid for rms values, we can see that the peak values are captured well compared with numerical data but the change is abrupt in our predictions. Also, we can say that numerical data (both our and Fureby's results) predict higher rms values than experimental results. Overall, our results show that capture effects of mesh resolution and reaction mechanism is negligible.

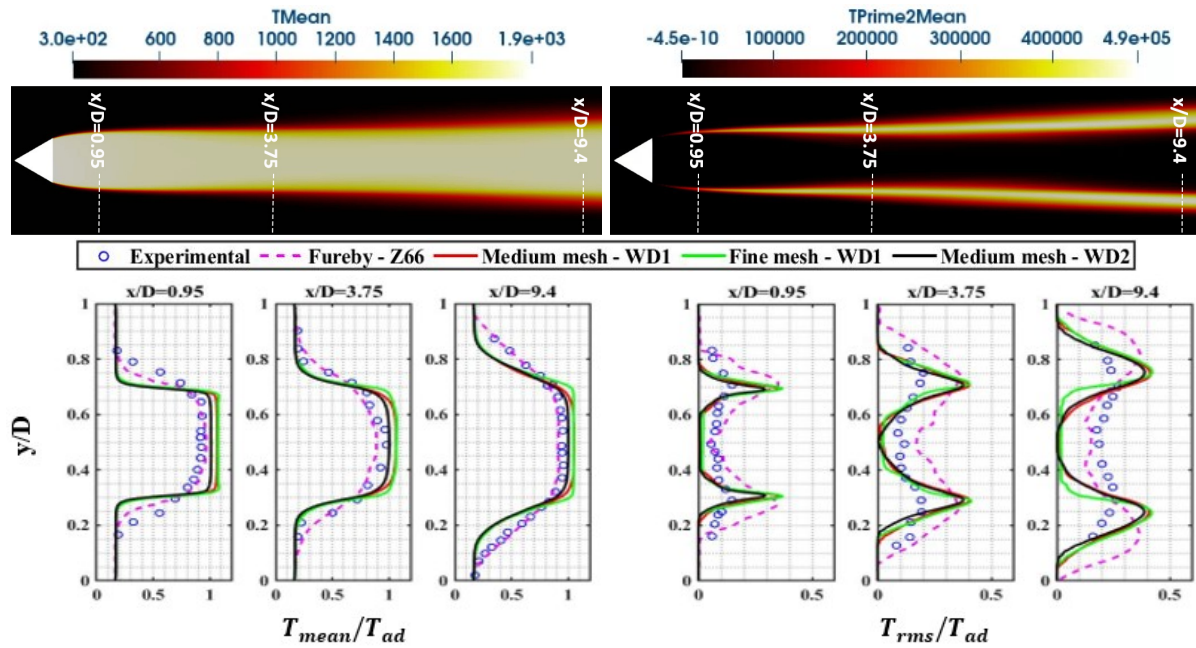


Figure 6: Top: Mean temperature (left) and rms (right) contour and sample lines. Bottom left: Normalized mean temperature distributions along the sample lines. Bottom right: Normalized rms temperature distributions along the sample lines.

Furthermore, velocity distributions are examined in five different stations. Results are compared to numerical and experimental data. The mean axial velocity distribution for both reacting and non-reacting flows is depicted in Figure 7. The re-circulation zone expands along the flow path because of the reaction. This effect can be observed in $x/D = 3.75$, non-reacting flow suppresses the re-circulation zone effect in this station, unlike reacting flow. Also at the last station, mean axial velocity values of reacting flow are much higher than the non-reacting flow because of the expansion and heat effect. As we can see from the figure, there are no crucial differences between meshes and reaction mechanisms, and all results agree well with both numerical data and experimental data.

The axial root-mean-square (rms) values of both reacting and non-reacting flows are presented in Figure 8. In the reacting flow, the axial rms value is significantly lower than the one in the non-reacting flow inside the re-circulation zone ($x/D = 0.375$). The acceleration of the flow due to the heat release suppresses the shear-layer instability and results in lower turbulent activity. This deviation between two cases decreases along the flow path direction. After the re-circulation zone, rms values are damped in the non-reacting flow. On the other hand, rms values of reacting flow increases at the exhaust of the combustor because of the heat and expansion effect. Lastly, same as in the mean axial velocity distribution, all meshes and reaction mechanisms give same results and all results agree well with numerical and experimental results.

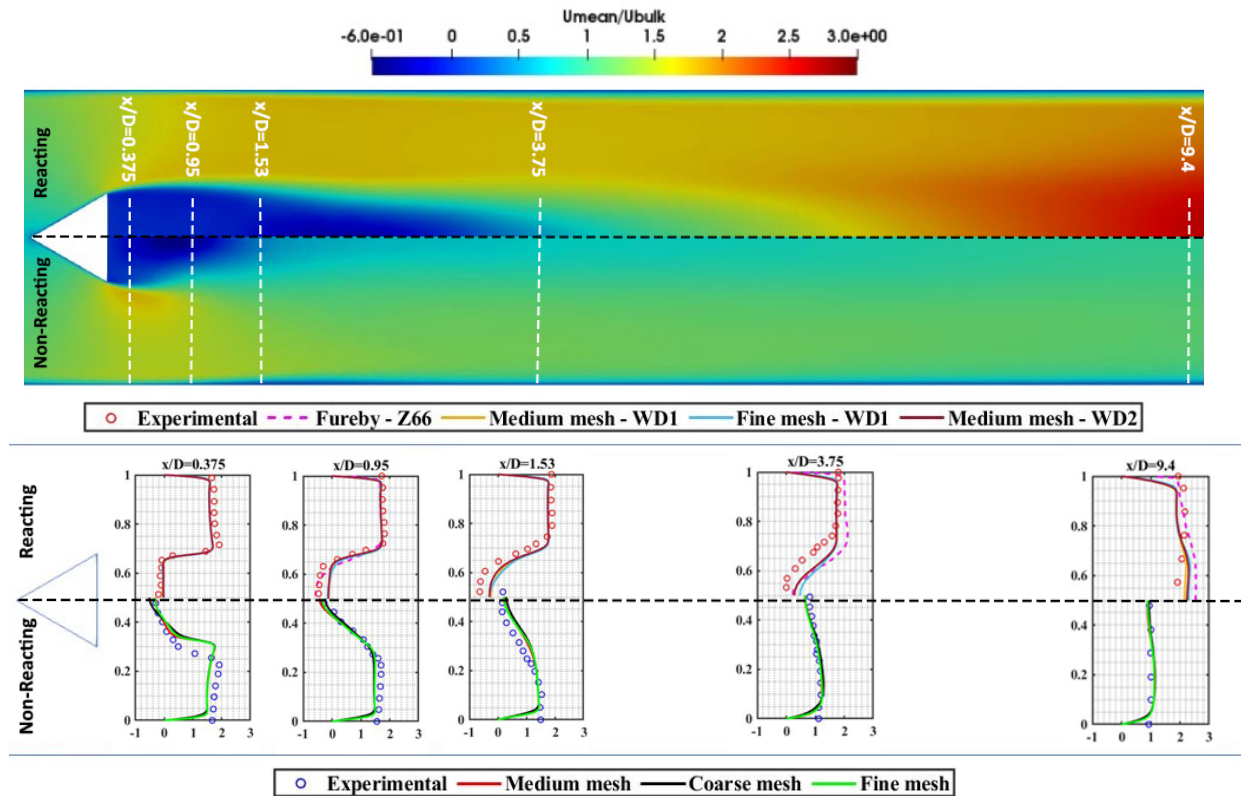


Figure 7: Top: Normalized mean axial velocity contour with streamlines and sample lines. Bottom: Normalized mean axial velocity distributions along the sample lines.

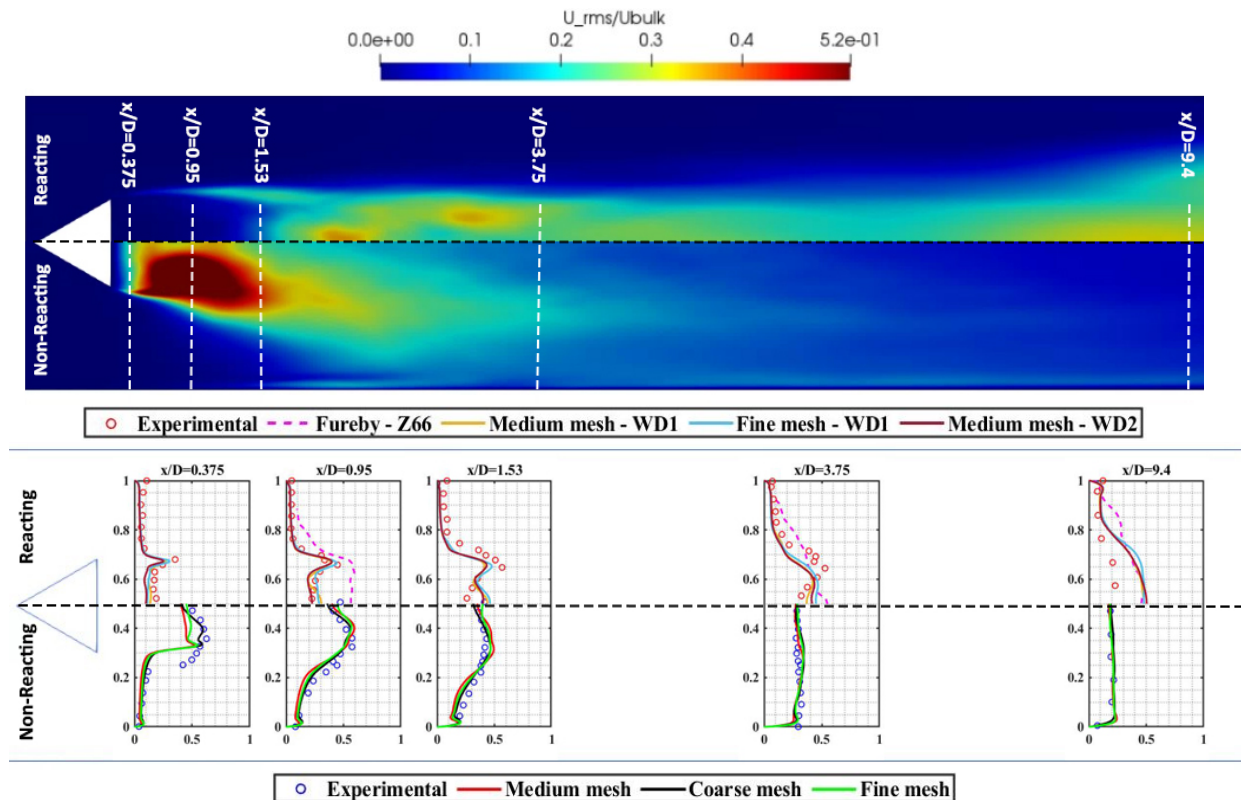


Figure 8: Top: Normalized axial rms velocity contour and sample lines. Bottom: Normalized axial rms velocity distributions along the sample lines.

The time-averaged CO mass fraction contour obtained with the two-step reaction mechanism, WD-2 at the mid plane and the distributions along some sample lines are shown in Figure 9 [Westbrook and Dryer, 1981] [Fureby, 2019]. The time-averaged mass fraction is expressed as a percentage when compared with the experimental data. Even though the LES results under-predicts the CO mass fraction distribution inside the combustor, there is still a strong coherence with the experimental data.

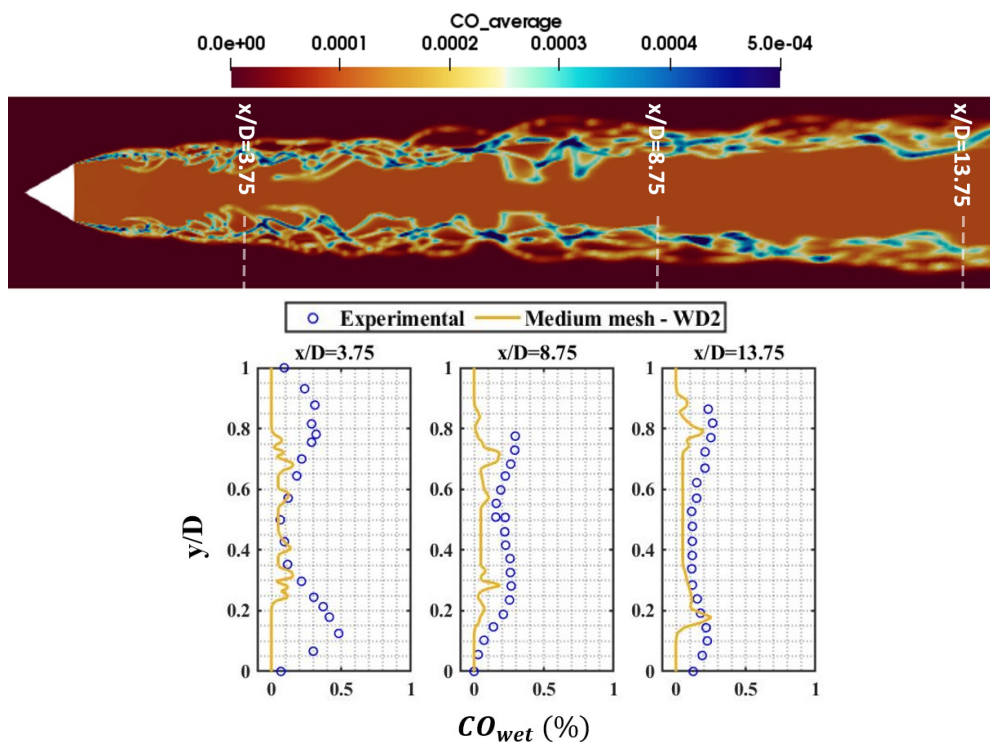


Figure 9: Top: CO mass fraction contour and sample lines. Bottom: CO mass fraction distributions along the sample lines.

CONCLUSION

Flow behind a bluff body geometry designed by AFRL is examined as reacting and non-reacting using an open source flow solver, OpenFOAM. LES method, in which large scales are solved and small scales are modeled, is employed in both analysis. The subgrid scale terms are modelled by Smagorinsky model. In order to model the reaction, PaSR combustion model is used in premixed propane-air combustion. In addition, one step and two-step global propane-air reaction mechanisms are conducted in order to examine the effect of reaction mechanism on the flame.

Accuracy of the analysis and the competency of the mesh resolution and reaction mechanisms are evaluated in terms of vortex shedding frequency, mean and rms axial velocity and temperature distributions. In the lights of these assessments, it is observed that all results agree well with experimental and numerical data for both non-reacting and reacting flows.

Reacting flow has a larger re-circulation zone along the flow path, compared to non-reacting flow. Furthermore results show that the reaction suppresses the Kelvin-Helmholtz instability and wall-vortex interaction.

Overall results show that two-step global reaction mechanism provides slightly better results than the one-step mechanism especially in terms of temperature but there are no crucial differences for the velocity field are observed between both reaction mechanisms. Despite the advantage of the two-step reaction mechanism to calculate the CO mass fraction, one-step mechanism was deemed more useful due to an excessive CPU-time usage.

According to the results, it is observed that there are no crucial differences between all generated meshes and reaction mechanisms. Even though the simple combustion model and global reaction mechanisms are used, the reaction effect on the flow is captured correctly. Further studies will evaluate the effect of combustion models on flow dynamics.

Acknowledgement

Computing resources used in this work were provided by the National Center for High Performance Computing of Turkey (UHem).

References

- AIAA SciTech (2020) *4th Model Validation for Propulsion Workshop Overview and Validation Case*, <https://community.aianet.org/wg/afrcg/mvpws>
- AIAA SciTech (2018) *2nd Model Validation for Propulsion Workshop Overview and Validation Case*, <https://community.aianet.org/wg/afrcg/mvpws>
- Bai, X., Fuchs, L. (1994) *Modeling of Turbulent Reactive Flows Past a Bluff Body: Assessment of Accuracy and Efficiency*, Computers and Fluids, Vol. 23, pp: 507–521.
- Bulat, G., Fedina, E., Fureby, C., Meier, W., Stopper, U. (2015). *Reacting flow in an industrial gas turbine combustor: LES and experimental analysis*, Proceedings of the Combustion Institute. Vol. 35, pp: 3175-3183.
- Ferrarotti, Z.Li.M., Cuoci, A., Parente, A. (2018) *Finite-rate chemistry modelling of non-conventional combustion regimes using a Partially-Stirred Reactor closure: Combustion model formulation and implementation details*, Applied Energy 225 (2018) 637–655.
- Fugger, C.A., Paxton, B.T., Gord, J.R., Rankin, B.A., and Caswell, A.W. (2019) *Measurements and Analysis of Flow-Flame Interactions in Bluff-Body-Stabilized Turbulent Premixed Propane-Air Flames*, AIAA Scitech 2019 Forum, San Diego, California, United States, AIAA 2019-0733.
- Fureby, C. (2019) *A Large Eddy Simulation (LES) Study of the VOLVO and AFRL Bluff Body Combustors at Different Operating Conditions*, IAA Scitech 2019 Forum.
- Giacomazzi E., Battaglia V., Bruno C., (2004) *The coupling of turbulence and chemistry in a premixed bluff-body flame as studied by LES*, Combustion & Flame 138 (4) 320-335.
- Iavarone, S., Péquin, A., Chen, Z., Doan, N.A.K., Swaminathan, N., Parente, Alessandro. (2020) *An a priori assessment of the Partially Stirred Reactor (PaSR) model for MILD combustion.*, Proceedings of the Combustion Institute. 38, pp: 2-3
- Lefebvre, A. H., Ballal, D. R. (2010) *Gas Turbine Combustion: Alternative Fuels and Emissions*, Third Edition, CRC Press.
- Manickam, B., Franke, J., Muppala, S.P.R., Dinkelacker, F. (2012) *Large-eddy Simulation of Triangular-stabilized Lean Premixed Turbulent Flames: Quality and Error Assessment*, Flow Turbulence Combust., Vol. 88, pp: 563–596.
- Poinsot, T., Veynate, D. (2012) *Theoretical and Numerical Combustion*, 3rd ed. isbn: 9782746639904, R.T. Edwards, Inc.

- Pope, S.B., Kim, J.(2014) *Effects of combined dimension reduction and tabulation on the simulations of a turbulent premixed flame using a large-eddy simulation/probability density function method*, Combust. Theory Model. Vol. 18, pp: 388–413.
- Porumbel I., Menon S., (2006) *Large Eddy Simulation of Bluff Body Stabilized Premixed Flames in Vitiated Crossflow*, 44th AIAA Aerospace Science Meeting and Exhibit, AIAA 2006-53
- Sabelnikov, V., Fureby, C. (2013) *Extended LES-PaSR model for simulation of turbulent combustion*, UCASS Proceedings Series. 4.
- Salvador, N. M. C., Mendonça, M. T. D., Dourado, W. M. D. C. (2013) *Large Eddy Simulation of Bluff Body Stabilized Turbulent Premixed Flame*, Journal of Aerospace Technology and Management, Vol.5, pp: 181–196.
- Sjunnesson A., Henrikson P., Löfström C. (1992) *Cars measurements and visualization of reacting flows in a bluff body stabilized flame*, AIAA/ASME/SAE/ASEE 28th Joint Propulsion Conference and Exhibit, AIAA 92-3650.
- Tovar, J. M. (2015) *Advances in Turbulent Combustion Dynamics Simulations in Bluff-Body Stabilized Flames*. [Master's Thesis, University of California]
- Westbrook, C. K., Dryer, F. L. (1981) *Simplified Reaction Mechanisms for the Oxidation of Hydrocarbon Fuels in Flames.*, Combustion Science and Technology, 27(1–2), 31–43.
- Yoder, D., DeBonis, J., & Georgiadis., N. (2015) *Modeling of turbulent free shear flows*. *Computers and Fluids*, Vol. 117, pp: 212–232.
- Zettervall, N., Nordin-Bates, K., Nilsson, E., Fureby, C. (2017) *Large Eddy Simulation of a premixed bluff body stabilized flame using global and skeletal reaction mechanisms.*, Combustion and Flame, Vol.179, pp: 1–22.